




Geophysical Research Letters[®]

RESEARCH LETTER

10.1029/2022GL101070

Localized Origin at the Core-Mantle Boundary of the 1969 Geomagnetic Impulse

R. M. Blangsbøll¹ , C. C. Finlay¹ , and C. Kloss¹ 

¹DTU Space, Technical University of Denmark, Kongens Lyngby, Denmark

Key Points:

- The 1969 impulse originated under central and North America as a north-south oriented localized dipole of field acceleration change
- It was preceded by a localized surge in secular variation and field acceleration patterns moved poleward during the event
- We suggest it was caused by a burst of vigorous convection close to the core surface which triggered flux expulsion and hydromagnetic waves

Supporting Information:

Supporting Information may be found in the online version of this article.

Correspondence to:

C. C. Finlay,
cfinlay@space.dtu.dk

Citation:

Blangsbøll, R. M., Finlay, C. C., & Kloss, C. (2022). Localized origin at the core-mantle boundary of the 1969 geomagnetic impulse. *Geophysical Research Letters*, 49, e2022GL101070. <https://doi.org/10.1029/2022GL101070>

Received 31 AUG 2022

Accepted 18 NOV 2022

Author Contributions:

Conceptualization: C. C. Finlay
Data curation: R. M. Blangsbøll, C. Kloss
Funding acquisition: C. C. Finlay
Investigation: R. M. Blangsbøll, C. C. Finlay, C. Kloss
Methodology: C. C. Finlay, C. Kloss
Project Administration: C. C. Finlay
Software: R. M. Blangsbøll, C. Kloss
Supervision: C. C. Finlay
Validation: R. M. Blangsbøll, C. C. Finlay, C. Kloss
Visualization: R. M. Blangsbøll, C. Kloss
Writing – original draft: R. M. Blangsbøll

© 2022. The Authors.

This is an open access article under the terms of the [Creative Commons Attribution License](https://creativecommons.org/licenses/by/4.0/), which permits use, distribution and reproduction in any medium, provided the original work is properly cited.

Abstract The 1969 geomagnetic impulse provided the first compelling evidence for rapid changes in Earth's core-generated magnetic field, taking place on timescales of a few years or less. We show here it originated at the core-mantle boundary (CMB) largely as a localized change in the field acceleration under north and central America. We find the impulse events in 1969 and 2017 involved similar amplitudes of field acceleration change with similar localized dipole structures. However in 1969 the acceleration change pattern was north-south rather than east-west oriented, and it propagated poleward rather than westward. Moreover, there was a distinctive local surge in the CMB secular variation leading up to the 1969 event. We propose the 1969 impulse resulted from hydromagnetic waves arriving at the CMB that were triggered by a convective burst near to the core surface; this event involved localized flux expulsion and inward propagating waves.

Plain Language Summary The 1969 geomagnetic impulse, an abrupt change in the core-generated geomagnetic field that occurred within just a few years, was crucial in convincing researchers that rapid dynamics are taking place in Earth's core. Here we reanalyze ground and satellite magnetic data collected around the time of this event, using modern field modeling and analysis techniques. We find the impulse originated at the core-mantle boundary (CMB) primarily as a change in the pattern of the field acceleration under north and Central America. We report evidence for a related localized increase in the amplitude of the first time derivative of the field, the secular variation, under north and Central America leading up to 1969. We also find that the field acceleration pattern moved poleward during the event. We propose these features can be understood if the impulse was triggered by convection close to the CMB that pushed field lines outwards across the boundary and triggered waves in the magnetic field which traveled inward into the core as columnar disturbances.

1. Introduction

Geomagnetic impulses, also known as geomagnetic jerks, are abrupt sign changes in the second time derivative (acceleration) of the geomagnetic field (Brown et al., 2013; Courtillot et al., 1978; Malin et al., 1983; Mandea et al., 2010). They are a well-known feature of magnetic observatory records, appearing as “V” or “inverted V” shapes in time series of the first time derivative or secular variation (SV). Impulses have been observed in all field components and, during some events, are observed almost simultaneously at remote locations at Earth's surface (Alexandrescu et al., 1996; Pinheiro et al., 2011). They carry information on rapid core processes responsible for reorganizing the gradual evolution of the field and are the main obstacle to obtaining accurate predictions of the future field, years to decades ahead.

Satellite magnetic field observations over the past two decades have provided us with a new, truly global yet detailed, picture of geomagnetic field evolution (Baerenzung et al., 2022; Lesur et al., 2010; Olsen et al., 2006). We are now able to map large scale patterns of geomagnetic secular acceleration (SA) at the core-mantle boundary (CMB) and their time changes (Lesur et al., 2008; Olsen & Mandea, 2008). Geomagnetic impulse events have been identified during this period, for example, in 2003 (Olsen & Mandea, 2007), 2014 (Torta et al., 2015) and 2017 (Finlay et al., 2020). It has been shown these originate at the CMB as localized patches of intense SA that rapidly change sign during an impulse (Chulliat & Maus, 2014; Chulliat et al., 2010; Finlay et al., 2015). These rapidly changing intense SA patches are most prominent in the equatorial region, and they have been observed to drift at speeds much larger than the advection speed in the core (Chulliat et al., 2015; Chulliat & Maus, 2014). Core flow inversions suggest they are associated with sign changes in the azimuthal component of the core flow acceleration (Gillet et al., 2015; Kloss & Finlay, 2019) and they appear to be consistent with hydromagnetic waves arriving at the CMB at low latitudes (Aubert & Finlay, 2019; Aubert et al., 2022; Gillet et al., 2022).

Writing – review & editing: C. C. Finlay, C. Kloss

There has however been some debate as to whether the rather localized impulses observed over the past 20 years belong to the same class of events as earlier impulses including an iconic event that happened in 1969. Here we perform a detailed reassessment of the 1969 impulse and its origin at the CMB, using modern field modeling techniques and analysis tools, compare it in detail with the well characterized 2017 event, and discuss consequences for our understanding of the rapid core processes.

2. Geomagnetic Observations

The primary data available to study the 1969 impulse are ground observatory measurements. Beginning with hourly mean measurements from the BGS AUX_OBS database (Macmillan & Olsen, 2013), which includes World Data Center holdings, we applied the “Revised Monthly Mean” processing scheme (Olsen et al., 2014). This involves first subtracting estimates of the magnetospheric and ionospheric fields and their induced counterparts. Regarding the magnetospheric field, we use the CHAOS field model taking as input a specially developed version of the RC index (Olsen et al., 2014) for 1960–1980 based on the stations: API, BJI, CLF, FRD, GUA, GNA, HAD, HER, HON, KAK, KYN, ODE, PMG, RSV, SJG, and TUC. Regarding the ionospheric field, we use the ionospheric part of the CM4 model (Sabaka et al., 2004) driven by F10.7 between 1960 and 1980. A robust (Huber) mean of the corrected hourly mean values is then carried out for each vector field component each month. SV estimates are obtained by taking annual differences.

Examples of the resulting SV time series clearly showing the 1969 impulse in the radial field component in San Juan, Puerto Rico (“SJG”), the southward field component at Fredericksburg, USA (“FRD”), and the eastward field component at Niemegk, Germany (“NGK”) are presented in Figures 1a–1c. We allocate error estimates to each field component at each observatory based on RMS residuals compared to the CM4 field model. We account for error covariances between field components. In all, we use data from 130 ground observatories, that operated at some time between 1960 and 1980, see Figure 1d. At least 70 ground observatories recorded data each month, with an average of 80 observatories operating after 1965.

In addition to ground measurements we use satellite measurements of the absolute intensity of the magnetic field F (i.e., scalar only measurements) from OGO-2, OGO-4, and OGO-6, known collectively as the POGO satellites (Langel, 1974). OGO-2 operated from October 1965 to November 1967 with large data gaps, due to power supply problems. OGO-4 operated from July 1967 to October 1969 and OGO-6 from June 1969 until June 1971. The major limitation of POGO data is imprecise positions due to the poor tracking abilities and the rudimentary gravitational models at this time, which results in an error budget of ± 25 nT (Stockmann et al., 2015). Due to their elliptical orbits OGO-2 had an altitude range of ≈ 400 –1600 km, OGO-4 ≈ 400 –1000 km, and OGO-6 ≈ 400 –1100 km.

We implemented geomagnetic quiet time and dark selection criteria to identify POGO data suitable for field modeling. Starting with a 30 s data sampling, we selected data only for time periods when the Kp index (Matzka et al., 2021) was less than 2° and the magnitude of the rate of change of the RC index (Olsen et al., 2014) was less than 2 nT/hr. To avoid the strongest dayside SQ currents we used only data when the zenith angle of the satellite location was greater than 70° . Gross outliers departing more than ± 300 nT from the CM4 field model were removed. The resulting temporal distribution of the POGO data is presented in Figure 1e. There are obvious gaps especially for OGO-2, some overlap in data coverage between OGO-2 and -4, and a gap of a few months between OGO-4 and -6. In addition to scalar field measurements themselves we also used their along-track differences at intervals of 30 s. Along-track differences are more sensitive to small scale field features and less affected by the large-scale magnetospheric field and have proved useful for high resolution modeling of the internal field (Olsen et al., 2015).

3. Methodology

We follow, with a few modifications, the modeling strategy used to construct the CHAOS series of high resolution geomagnetic field models (Finlay et al., 2020; Olsen et al., 2006, 2014). Assuming the current density in the region of study is small, and field time changes are slow, we write the vector magnetic field $\mathbf{B} = -\nabla V$ where V is a scalar potential. Since the magnetic field is divergence-free, V is a solution of Laplace’s equation and in spherical geometry can be decomposed into two parts, V^{int} , representing internal sources, and V^{ext} , representing external sources. We focus below on internal sources described by

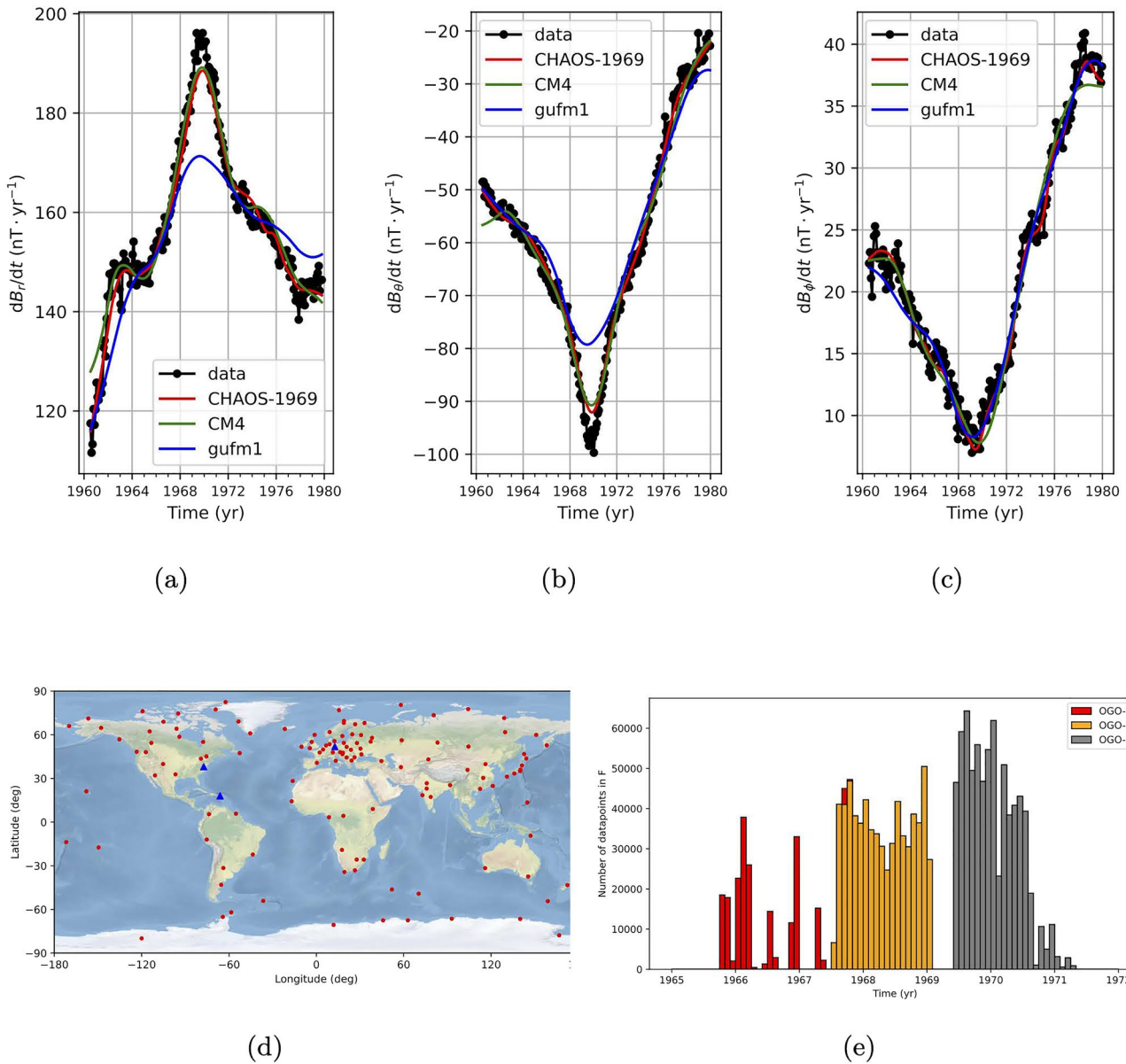


Figure 1. (a–c) Annual differences of revised monthly means (denoted as “data”), at ground observatories SJK (San Juan, USA), FRD (Fredericksburg, USA), and NGK (Niemegk, Germany) of the radial, southward, and eastward field components, respectively, with the CHAOS-1969, CM4 and *gufm1* field models shown for comparison, all truncated at spherical harmonic degree 12. (d) Plot of ground observatory locations, with SJK, FRD, and NGK marked in blue, and (e) Stacked histogram of number of scalar field intensity (F) data per month from the OGO-2, -4, and -6 satellites used in this study.

$$V^{\text{int}}(r, \vartheta, \phi, t) = a \sum_{n=1}^{N_{\text{int}}} \sum_{m=0}^n \left(\frac{a}{r}\right)^{n+1} [g_n^m(t) \cos m\phi + h_n^m(t) \sin m\phi] P_n^m(\cos \vartheta) \quad (1)$$

where $a = 6371$ km is Earth's mean spherical radius, (r, ϑ, ϕ) are the geographic coordinates, t is time, P_n^m are Schmidt semi-normalized associated Legendre functions of degree n and order m , and $\{g_n^m, h_n^m\}$ are known as the Gauss coefficients. The model reported here, which we refer to as CHAOS-1969, is time-dependent up to $N_{\text{int}} = 13$ and uses a basis of sixth order B-splines running between 1960 and 1980 with a 6 months knot spacing. It also includes a static internal field fixed a priori to be that from the CHAOS-7.8 field model (Finlay et al., 2020) for degrees 21 to 60.

Regarding the external field, we adopt the same parameterization and truncation levels as in the CHAOS model series. Near-Earth magnetospheric sources are represented via an expansion in Solar Magnetic coordinates, with the time-dependence of the degree 1 terms parameterized using an RC index. Remote external sources in the magnetopause and tail regions are represented using an expansion in Geocentric Solar Magnetospheric coordinates (Laundal & Richmond, 2017). The related induced responses from a spherically symmetric conducting Earth are included, as described by Finlay et al. (2020). No Euler angles related to satellite orientation are needed as the satellite data is scalar only. The resulting model consists of 13,237 parameters, 12,495 describing the internal field and 742 the external field.

We estimate these parameters using 1,005,973 observations via a robust, iteratively reweighted, least squares algorithm including model regularization (Olsen, 2002; Olsen et al., 2006; Walker & Jackson, 2000). This involves iteratively minimizing an objective function of form:

$$\mathcal{J} = \mathbf{e}^T \underline{\underline{\mathbf{W}}} \mathbf{e} + \lambda_3 \mathbf{m}^T \underline{\underline{\Lambda}}_3 \mathbf{m} + \lambda_2 \mathbf{m}^T \underline{\underline{\Lambda}}_2 \mathbf{m} + \lambda_0 \mathbf{m}^T \underline{\underline{\Lambda}}_0 \mathbf{m} \quad (2)$$

where $\mathbf{e} = \mathbf{d}_{\text{obs}} - \mathbf{g}(\mathbf{m})$ is the vector of residuals, observations minus the model predictions. $\underline{\underline{\mathbf{W}}} = \underline{\underline{\mathbf{C}}}^{-1/2} \underline{\underline{\mathbf{H}}} \underline{\underline{\mathbf{C}}}^{-1/2}$ is a data weight matrix derived from an a-priori data error covariance matrix, $\underline{\underline{\mathbf{C}}}$, which includes off-diagonal terms between field components at each ground observatory, and with $\underline{\underline{\mathbf{C}}}^{-1/2}$ denoting square root factors of its inverse, and $\underline{\underline{\mathbf{H}}}$ is a diagonal matrix of residual-dependent weights based on a Huber error distribution (Constable & Parker, 1988). $\mathbf{m}^T \underline{\underline{\Lambda}}_3 \mathbf{m}$ is a quadratic norm measuring the mean squared magnitude of the third time derivative of the radial field, $\left| \frac{\partial^3 B_r}{\partial t^3} \right|$, integrated over the CMB and averaged over the model timespan. $\mathbf{m}^T \underline{\underline{\Lambda}}_2 \mathbf{m}$ is a similar measure of the mean square magnitude of the second time derivative (secular acceleration) of the radial field at the CMB, $\left| \frac{\partial^2 B_r}{\partial t^2} \right|$, evaluated only at the endpoints of the model. $\mathbf{m}^T \underline{\underline{\Lambda}}_0 \mathbf{m}$ measures the mean square magnitude of the radial field integrated over the CMB and averaged over the model timespan; it is included in order to help control the Backus effect (Backus, 1970; Holme et al., 2005). λ_3 , λ_2 , and λ_0 are adjustable regularization parameters associated with these three norms, chosen to ensure a suitable balance between fitting rapid time variations at ground observatories and controlling spurious variations related to varying data constraints and end effects.

Due to the use of scalar intensity data and Huber weights that depend on the model, Equation 2 is a non-linear function of the model parameters. We minimize it by linearizing and by using a Newton-type scheme, iteratively updating the model parameters until convergence according to

$$\begin{aligned} \mathbf{m}_{i+1} &= \mathbf{m}_i + \delta \mathbf{m}_i \\ \text{where } \delta \mathbf{m}_i &= \left[\underline{\underline{\mathbf{G}}}_i^T \underline{\underline{\mathbf{W}}} \underline{\underline{\mathbf{G}}}_i + \lambda_3 \underline{\underline{\Lambda}}_3 + \lambda_2 \underline{\underline{\Lambda}}_2 + \lambda_0 \underline{\underline{\Lambda}}_0 \right]^{-1} \\ &\quad \cdot \left[\underline{\underline{\mathbf{G}}}_i^T \underline{\underline{\mathbf{W}}} (\mathbf{d}_{\text{obs}} - \mathbf{g}(\mathbf{m}_i)) - \lambda_3 \underline{\underline{\Lambda}}_3 \mathbf{m}_i - \lambda_2 \underline{\underline{\Lambda}}_2 \mathbf{m}_i - \lambda_0 \underline{\underline{\Lambda}}_0 \mathbf{m}_i \right] \end{aligned} \quad (3)$$

and $\underline{\underline{\mathbf{G}}}_i = \left. \frac{\partial \mathbf{g}(\mathbf{m})}{\partial \mathbf{m}} \right|_{\mathbf{m}=\mathbf{m}_i}$ is the Jacobian matrix of partial derivatives with respect to the model parameters. The model was considered converged when the L2 norm of the data misfit changed less than 10^{-4} from the previous iteration, which was satisfied after 7 iterations.

4. Results

We report here results from our new field model spanning 1960 to 1980, called CHAOS-1969, derived using the data set and method described above. Regularization parameters were set to values of $\lambda_3 = 0.1 \text{ (nT days}^{-3}\text{)}^{-2}$, $\lambda_2 = 0.002 \text{ (nT days}^{-2}\text{)}^{-2}$, and $\lambda_0 = 2.5 \times 10^{-7} \text{ (nT)}^{-2}$ which we found allowed sharp field changes associated with the 1969 impulse to be captured, whilst minimizing spurious oscillations in SV time series and mitigating the Backus effect. The RMS misfit to the POGO non-polar scalar intensity data was 4.75 nT for OGO-2, 5.77 nT for OGO-4 and 22.88 nT for OGO-6, and 9.47, 6.80, and 6.03 nT/yr respectively for the radial, southward and eastward components of ground observatory SV series. Example comparisons of the CHAOS-1969 model to observatory SV series where the 1969 impulse is clearly seen are shown in Figure 1. Similar Figures for all observatories where the impulse was evident are shown in Text S5 in Supporting Information S1.

Global maps of the CMB radial magnetic field structure, and its time derivatives, at the time of the 1969 impulse, are presented in Figure 2. In these and subsequent figures, maps were produced by truncating the models such that their CMB power spectra were found to be well behaved, at spherical harmonic degree 13 for the field, 12 for the SV, and 8 for the SA, respectively (see Text S2 of Supporting Information S1). The CMB field and its SV show structures familiar from previous field models covering the historical and satellite eras (Holme et al., 2011; Jackson et al., 2000). One noteworthy feature is a north-south oriented, positive-negative, pair of SV patches under the Caribbean and eastern North America in Figure 2b. These are not seen in maps of the more recent CMB SV but have been noted in previous models of this period (Dormy & Manda, 2005; Jackson et al., 2000; Sabaka et al., 2004); we shall return to them later. Figures 2c and 2d show the morphology of the SA at the CMB averaged over 1966.75 to 1969.75 and 1969.75 to 1972.75, that is over 3 years before and after the 1969 impulse. Despite the power spectra of the SA at the CMB increasing with degree these maps provide important information on the dynamical processes underlying observed field changes (Aubert et al., 2022).

Our main result, the CMB origin of the 1969 impulse, is presented in Figure 2e. This shows the change in the radial field SA at the CMB across the impulse, which we calculate as

$$\Delta \ddot{B}_r(c, \vartheta, \phi, t_0) = \frac{1}{\Delta T} \int_{t=t_0}^{t_0+\Delta T} \ddot{B}_r(c, \vartheta, \phi, t) dt - \frac{1}{\Delta T} \int_{t=t_0-\Delta T}^{t_0} \ddot{B}_r(c, \vartheta, \phi, t) dt \quad (4)$$

where c is the CMB radius, t_0 is the impulse time which we take as 1969.75 and $\Delta T = 3$ years is a time-averaging interval, before and after the impulse, during which there was a consistent SV trend (SA). Figure 2e shows this $\Delta \ddot{B}_r$ for the 1969 impulse, calculated by differencing the time-averaged SA maps shown in Figures 2c and 2d. We find the 1969 impulse was dominated by a striking local dipole of intense radial field SA change under the Caribbean and North America. This feature is also seen in models built with POGO data alone, in models built with key observatories removed and in the CM4 model (see Texts S1 and S3 in Supporting Information S1).

The relation between $\Delta \ddot{B}_r(c, \vartheta, \phi, t_0)$ and changes in the slope of SV (i.e., changes in the time-averaged SA) at ground observatory locations $\Delta \ddot{\mathbf{B}}(\mathbf{r})$ is given by Green's functions that link the potential field at Earth's surface to its internal sources, specified by Neumann boundary conditions as the radial field at the CMB (Gubbins & Roberts, 1983; Hammer & Finlay, 2018).

$$\Delta \ddot{\mathbf{B}}(\mathbf{r}) = \int_{CMB} \mathbf{G}(\mathbf{r}, \hat{\mathbf{s}}) \Delta \ddot{B}_r(\hat{\mathbf{s}}) dS \quad (5)$$

where dS is a surface element at the CMB, and $\mathbf{G} = \{G_r, G_\theta, G_\phi\}$ are directional derivatives of the Green's functions, or functions of sensitivity, that link the radial field at the CMB, $B_r(\hat{\mathbf{s}})$, to the spherical polar vector components of the field, $\{B_r(\mathbf{r}), B_\theta(\mathbf{r}), B_\phi(\mathbf{r})\}$. Explicit expressions for G_r, G_θ, G_ϕ can be found in Hammer and Finlay (2018) Equations 3–5. They show how the radial field at each location at the CMB contributes to a given component of the field at a chosen site on Earth's surface.

Figures 2f–2h show $\Delta \ddot{B}_r$ at the CMB multiplied by the values of G_r for an observation at San Juan, G_θ for an observation at Fredericksburg, and G_ϕ for an observation at Niemegek respectively. Integrating these maps over the CMB gives the numbers indicated at the top of the plot which correspond to the predicted SA change in the relevant component at the specified site, according to the field model. SA changes calculated in this way agree well with those found from changes in the trend of the SV series in Figure 1. These maps enable us to pinpoint the SA changes at the CMB responsible for the 1969 impulse observed at ground observatories. For the radial component at SJG the largest contribution comes from directly below the observation point where there is a strong negative SA change on the CMB. For the southward component at Fredericksburg, locations to the south on the CMB contribute negatively, represented on the maps by dashed lines. This explains how the negative SA change under the Caribbean adds to positive SA change under North America to produce a net strong positive SA change at this location. For the eastward component in Niemegek, the primary contribution comes from the positive SA change feature under North America. In all three locations, the origin of the impulse is SA change under north and Central America. Similar maps for 35 other observatories where the 1969 impulse was clearly detected are presented in Text S5 of the Supporting Information S1.

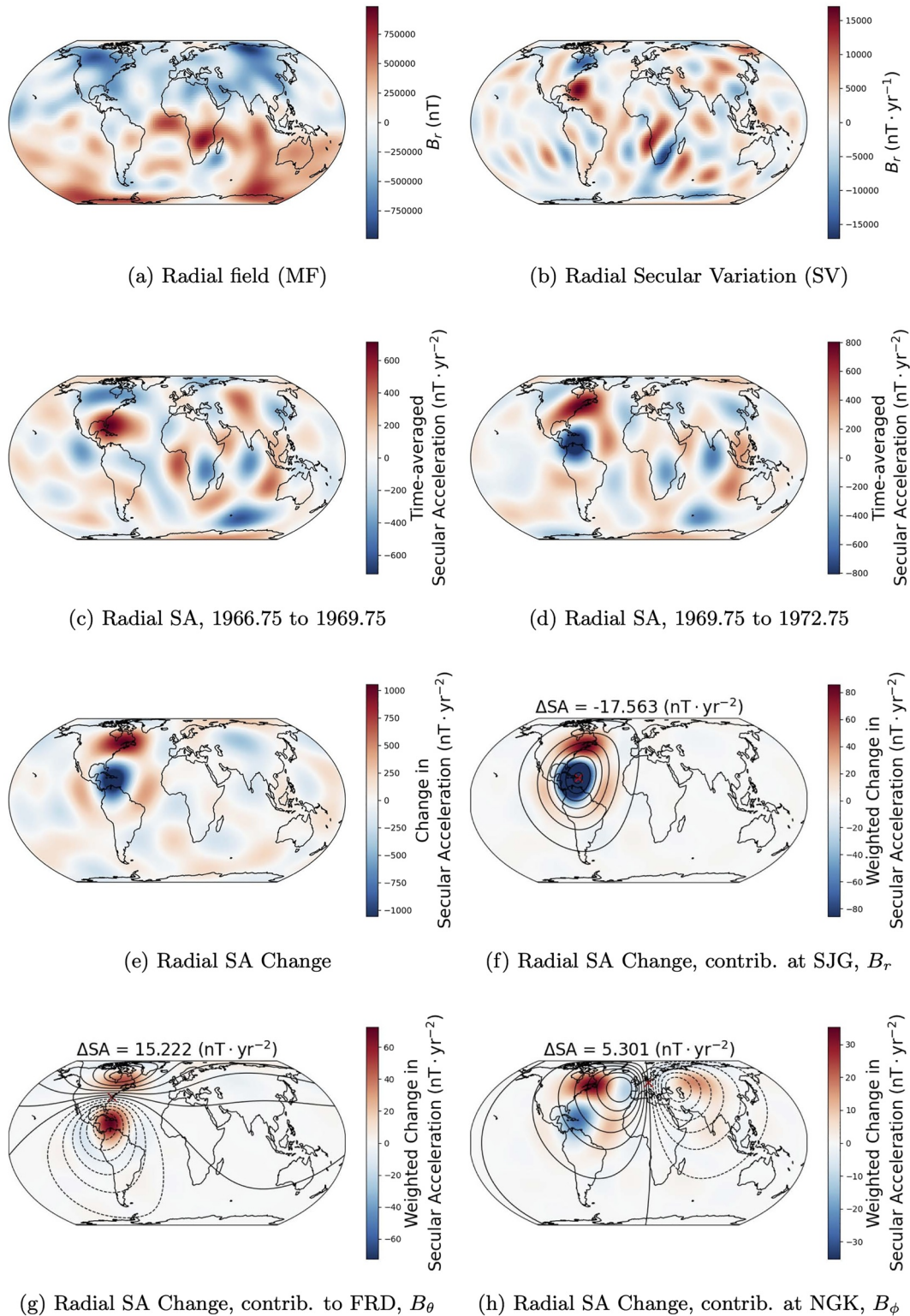


Figure 2. The CMB magnetic field (MF) and its changes during the 1969 geomagnetic impulse from the CHAOS-1969 field model. (a) Shows the radial component of the MF and (b) the radial field secular variation (SV) in September 1969, truncated at degree 13 and 12, respectively. (c and d) Show the CMB radial field secular acceleration (SA) time-averaged for 3 years preceding and after 1969.75 respectively, truncated at degree 8. (e) Shows the change in SA at the CMB associated with the 1969 impulse computed by differencing (c and d). (f–h) Show similar plots weighted with Greens functions (contours) for observations of the radial, southward and eastward directions at the SJG, FRD, and NGK observatories respectively. The associated SA change of the surface field is noted.

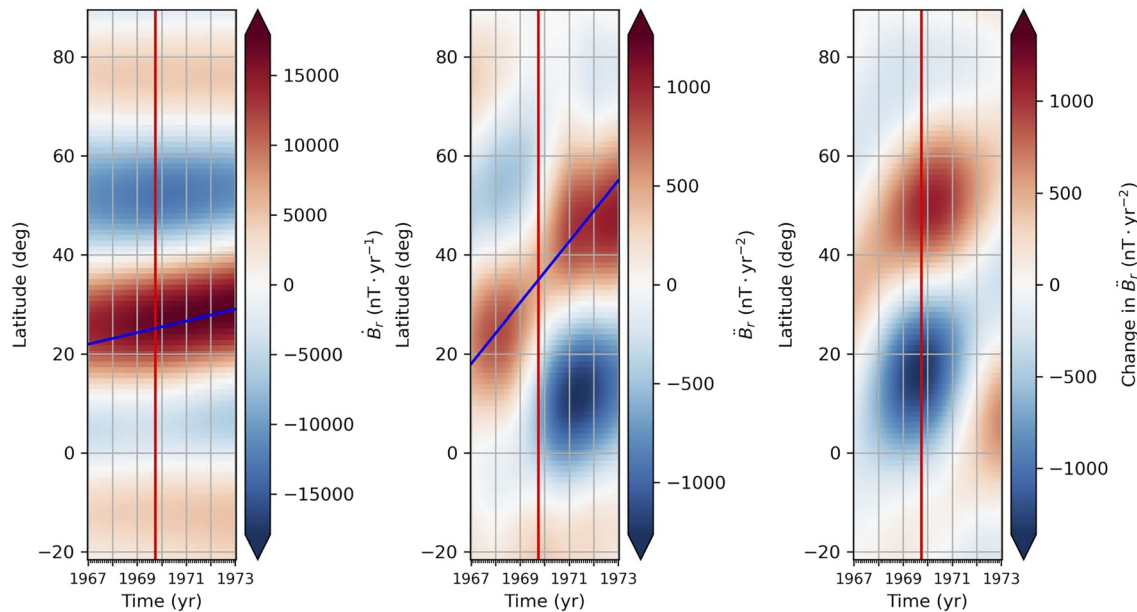


Figure 3. Time versus latitude plots at the CMB showing the field evolution in the northern hemisphere at longitude 68° west. Left: the radial field SV truncated at spherical harmonic degree 12, Center: SA truncated at spherical harmonic degree 8, Right: change in SA truncated at spherical harmonic degree 8. The 1969 impulse event is marked by the red line. Blue lines mark the typical latitudinal drift speed of the SV and SA patches, 1.17 deg/yr (71 km/yr) and 6.17 deg/yr (375 km/yr) respectively.

The time evolution of the SV and SA under central and North America is crucial to understanding the 1969 impulse. Figure 3 shows that the dipolar anomalies in the CMB SV and SA seen in Figures 2b–2d moved poleward. According to slopes marked in the time-latitude plots the CMB SV and SA features moved poleward with speeds of approximately 71 and 375 km/yr . The SA features also decreased in amplitude at the time of the impulse, when the SA change was largest. Poleward motion of the SV and SA features is also readily seen in animations of global maps similar to Figure 2 which are available as part of Supporting Information S1.

5. Discussion

The 1969 impulse is often characterized as worldwide in extent (Alexandrescu et al., 1996; Brown et al., 2013; Pinheiro et al., 2011). How can this be compatible with a localized origin at the CMB? First we note that impulse detections commonly attributed to the 1969 event in the vicinity of Australia and New Zealand occurred later, around 1972. In our opinion they are associated with a different arrival of energy at the CMB; this is consistent with previous studies of the links between impulses and changes in the length of day (Holme & de Viron, 2013). Of the 35 ground observatories that show the clearest impulses centered on 1969, only 5 cannot be explained in terms of the SA change under North America and the Caribbean (see Text S5 in Supporting Information S1 for the analysis of Figures 2f and 2g applied to all 35 stations). The 5 exceptions are all located in central and eastern Asia and are linked to a weaker patch of negative radial SA change at the CMB under central Asia in 1969, see in Figure 2e. Earlier studies of the 1969 impulse at Earth's surface (Le Huy et al., 1998; Sabaka et al., 2004) and the CMB (Pinheiro et al., 2011) also found prominent changes in the radial field acceleration under north and central America, but they also inferred relatively strong SA changes in Asia and the Indian ocean. With the improved spatial and temporal resolution of our new model, and based on our new methods of analysis, we find the latter features are not required to explain the 1969 impulse.

An important question that motivated this study is whether the classic 1969 impulse was fundamentally different from more recent impulses observed during the era of continuous satellite observations, for example, the 2017 Pacific impulse that has been characterized in detail by *Swarm* observations (Finlay et al., 2020; Hammer et al., 2022). Figure 4 presents a comparison of relevant aspects of these two impulses. Figures 4a and 4b show maps of radial field SA change at the CMB for each impulse, obtained by differencing the SA time-averaged

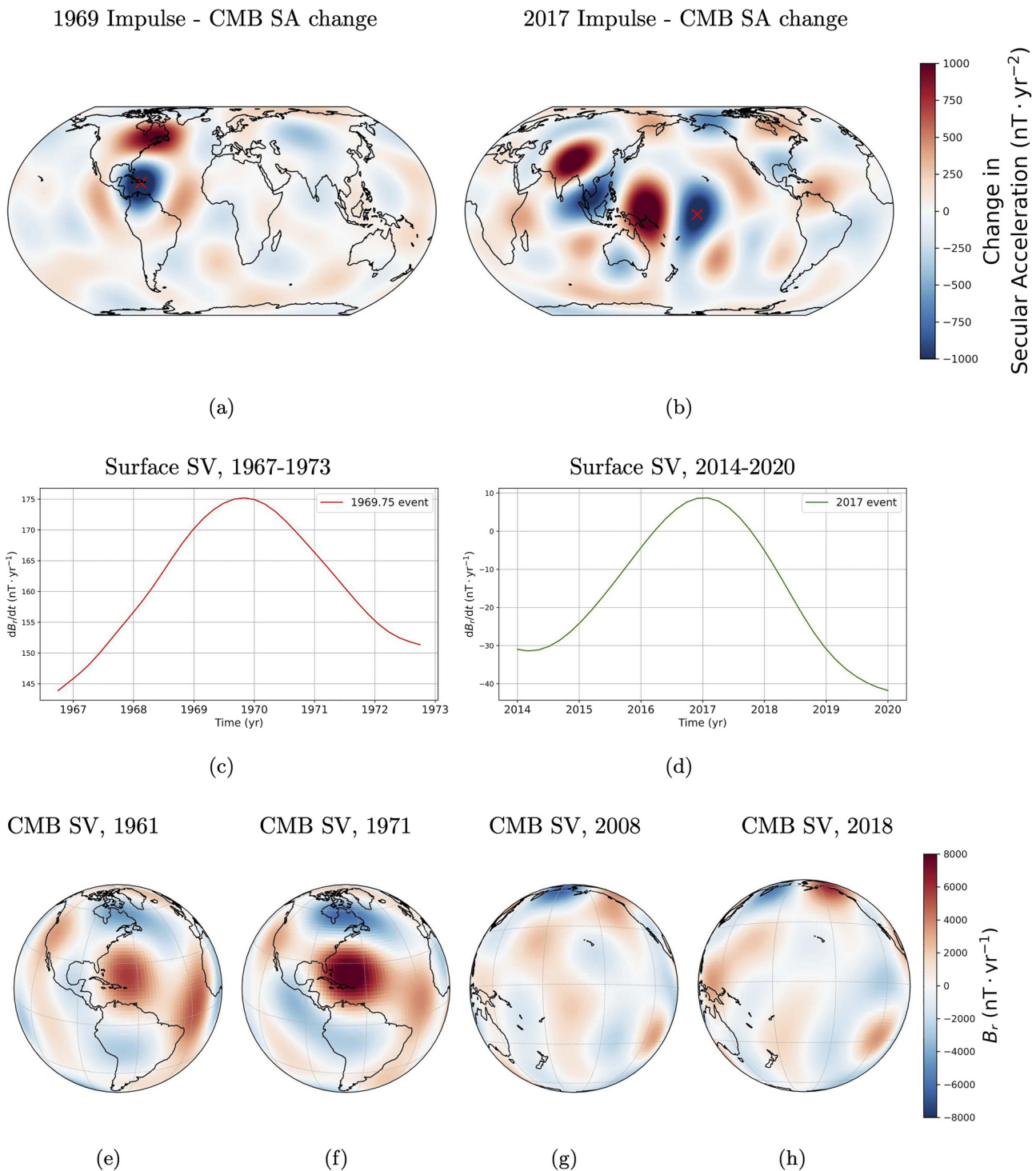


Figure 4. (a, b) Global maps of the change in the radial field SA of the CHAOS-1969 and CHAOS-7.8 models in target year 1969.75 and 2017 at the CMB with the chosen synthetic ground observatory marked. (c, d) The SV from the two chosen synthetic ground observatories. (e–h) Nearside perspective plots of the CMB SV, centered at the locations of maximum SA change, in (e) 1961 and (f) 1971 from the CHAOS-1969 model and in (g) 2008 and (h) 2018 from the CHAOS-7.8 model. All truncated at maximum spherical harmonic degree 8.

over 3 years before and after the impulse, as in Figure 2e. The amplitudes of the two impulses are similar and both involve localized dipolar patterns. In 2017 there are however two dipolar SA change structures visible - the strongest (and longer lived) feature is under the central Pacific and is oriented east-west, a second feature, of slightly smaller scale, is present under east Asia and more north-south oriented.

Figures 4c and 4d show the signatures of the two impulses in SV time series at Earth's surface. These are the signatures that would have been observed if ground observatories were located directly above the maximum amplitude of radial field SA change at the CMB, marked by the red x's in Figures 4a and 4b. "Inverted V" shapes are seen in both cases, with an increase and then decrease of the SV by 30–40 nT/yr occurring within 6 years as in the classic signatures presented in Figure 1. In terms of both the SA change at the CMB, and changes in SV trends at ground observatories, we find no evidence the 2017 impulse was of lower amplitude than the 1969 impulse.

An important difference between the 1969 and 2017 impulses does however become evident on examining maps of the CMB SV leading up to and during the events. In the decade leading up to the 1969 impulse there was a localized dipolar surge in the CMB SV under North America. This dipolar anomaly in the CMB SV is clearly visible in the global map of the CMB SV in 1969 shown in Figure 2b. Its development between 1961 and 1971 is illustrated in Figures 4e and 4f; the good coverage of ground observatories in this region means it can be accurately imaged already in the early 1960s. This localized feature is however too small to have much impact on the integrated SV power at Earth's surface; such global signatures have been found for some earlier impulses (Jackson, 1997; Jackson & Finlay, 2007). In contrast with the 1969 event, as shown in Figures 4g and 4h there was no CMB SV anomaly associated with the 2017 impulse.

The different signatures of the 1969 and 2017 impulses in the CMB SV may point to different triggering mechanisms. Aubert et al. (2022) have documented differences between impulses triggered by deep and shallow sources in their geodynamo simulations. In both cases oscillations in the core surface azimuthal flow, and localized dipolar patterns of change in CMB radial field SA, originate in rapid hydromagnetic waves generated by localized bursts of core convection. However, when the convective burst occurs near to the core surface, localized flux expulsion also takes place which generates a localized dipolar surge in the CMB SV. It seems possible that the 1969 impulse could therefore be an example of a shallow-triggered impulse while the 2017 event, which lacks a signature in the CMB SV, is more likely a deep-triggered impulse. Poleward motion of the SA patches seen in Figure 3 is consistent with a wave propagating into the core interior away from a source near the CMB. It is unclear whether the CMB location of the 1969 impulse and its related SV surge under North America, or the poleward motions of the associated SA patches, are somehow linked to the poleward leg of the planetary gyre and its fluctuations. There are intriguing indications in field models derived from historical records (Jackson et al., 2000) of enhanced SV and wave-like fluctuations of flux patches on decadal timescales in this region.

6. Conclusion

Analysis of a new field model derived from ground observatory and POGO satellite data focusing on the 1969 geomagnetic impulse shows it originated at the CMB in a north-south oriented localized dipole of radial field SA change. The responsible SA patches drifted rapidly poleward during the event. This feature explains the majority of the detections of the 1969 impulse, including famous observations in the eastward component in Europe and the radial and southward components in central and North America, thanks to the form of the Green's function that links the CMB radial field to surface observations.

The CMB SA change associated with the 1969 impulse has a similar amplitude and localized dipolar structure to the recently observed 2017 Pacific impulse. However the 1969 event was oriented north-south rather than east-west, and involved an SA pattern moving poleward rather than westward as was seen during the 2017 event.

A localized surge in the CMB SV leading up to the 1969 impulse may indicate it was triggered by a shallow source, close to the CMB (Aubert et al., 2022). However north-south oriented SV anomalies and the poleward motions of SA patterns are not seen in the present catalog of numerically simulated impulses. This may point to a different morphology of the underlying core magnetic field, or a different direction of the responsible convective burst, compared to that found in the simulations.

We focused here on the 1969 impulse since both satellite and ground observations were available to study it. It would be of great interest to learn more about the morphology of other well known jerk events, for example, the 1978 event, or the enigmatic 1914 event which appears to have been associated with a large surge in the globally integrated SV power at Earth's surface (Jackson, 1997). The latter likely required a much more dramatic CMB signature than that of the 1969 impulse studied here.

Data Availability Statement

The new geomagnetic field model derived during this study, CHAOS-1969, additional test models reported in Supporting Information S1, and the ground observatory and POGO satellite data used in the study, are available at https://data.dtu.dk/projects/Localized_origin_at_the_core-mantle_boundary_of_the_1969_geomagnetic_impulse/146112.

Acknowledgments

CCF and CK were supported by the European Research Council (ERC) under the European Union's Horizon 2020 research and innovation programme (Grant 772561). CCF also acknowledges support from the Swarm+ 4D Deep Earth: Core project, ESA contract no. 4000127193/19/NL/IA and thanks the members of this consortium for many helpful discussions.

References

- Alexandrescu, M., Gibert, D., Hulot, G., Le Mouél, J.-L., & Saracco, G. (1996). Worldwide wavelet analysis of geomagnetic jerks. *Journal of Geophysical Research*, 101(B10), 21975–21994. <https://doi.org/10.1029/96JB01648>
- Aubert, J., & Finlay, C. C. (2019). Geomagnetic jerks and rapid hydromagnetic waves focusing at Earth's core surface. *Nature Geoscience*, 12(5), 393–398. <https://doi.org/10.1038/s41561-019-0355-1>
- Aubert, J., Livermore, P. W., Finlay, C. C., Fournier, A., & Gillet, N. (2022). A taxonomy of simulated geomagnetic jerks. *Geophysical Journal International*, 231(1), 650–672. <https://doi.org/10.1093/gji/ggac212>
- Backus, G. (1970). Non-uniqueness of the external geomagnetic field determined by surface intensity measurements. *Journal of Geophysical Research*, 75(31), 6339–6341. <https://doi.org/10.1029/ja075i031p06339>
- Baerenzung, J., Holschneider, M., Saynisch-Wagner, J., & Thomas, M. (2022). Kalmag: A high spatio-temporal model of the geomagnetic field. *Earth Planets and Space*, 74, 139. <https://doi.org/10.1186/s40623-022-01692-5>
- Brown, W., Mound, J., & Livermore, P. W. (2013). Jerks abound: An analysis of geomagnetic observatory data from 1957 to 2008. *Physics of the Earth and Planetary Interiors*, 223, 62–76. <https://doi.org/10.1016/j.pepi.2013.06.001>
- Chulliat, A., & Maus, S. (2014). Geomagnetic secular acceleration, jerks, and a localized standing wave at the core surface from 2000 to 2010. *Journal of Geophysical Research: Solid Earth*, 119(3), 1531–1543. <https://doi.org/10.1002/2013jb010604>
- Chulliat, A., Alken, P., & Maus, S. (2015). Fast equatorial waves propagating at the top of the earth's core. *Geophysical Research Letters*, 42(9), 3321–3329. <https://doi.org/10.1002/2015gl064067>
- Chulliat, A., Thebaud, E., & Hulot, G. (2010). Core field acceleration pulse as a common cause of the 2003 and 2007 geomagnetic jerks. *Geophysical Research Letters*, 37(7), L07301. <https://doi.org/10.1029/2009gl042019>
- Constable, C. G., & Parker, R. L. (1988). Smoothing, splines and smoothing splines; their application in geomagnetism. *Journal of Computational Physics*, 78(2), 493–508. [https://doi.org/10.1016/0021-9991\(88\)90062-9](https://doi.org/10.1016/0021-9991(88)90062-9)
- Courtilot, V., Ducruix, J., & Le Mouél, J.-L. (1978). Sur une accélération récente de la variation séculaire du champ magnétique terrestre. *Comptes Rendus de l'Académie Des Sciences Paris D*, 287(12), 1095–1098.
- Dormy, E., & Manda, M. (2005). Tracking geomagnetic impulses at the core–mantle boundary. *Earth and Planetary Science Letters*, 237, 300–309. <https://doi.org/10.1016/j.epsl.2005.06.003>
- Finlay, C. C., Kloss, C., Olsen, N., Hammer, M. D., Tøffner-Clausen, L., Grayver, A., & Kuvshinov, A. (2020). The CHAOS-7 geomagnetic field model and observed changes in the south Atlantic anomaly. *Earth Planets and Space*, 72(1), 156. <https://doi.org/10.1186/s40623-020-01252-9>
- Finlay, C. C., Olsen, N., & Tøffner-Clausen, L. (2015). DTU candidate field models for IGRF-12 and the CHAOS-5 geomagnetic field model. *Earth Planets and Space*, 67(1), 114. <https://doi.org/10.1186/s40623-015-0274-3>
- Gillet, N., Barrois, O., & Finlay, C. C. (2015). Stochastic forecasting of the geomagnetic field from the COV-OBS.x1 geomagnetic field model, and candidate models for IGRF-12. *Earth Planets and Space*, 67(1), 71. <https://doi.org/10.1186/s40623-015-0225-z>
- Gillet, N., Gericke, F., Jault, D., Schwaiger, T., Aubert, J., & Istan, M. (2022). Satellite magnetic data reveal interannual waves in earth's core. *Proceedings of the National Academy of Sciences*, 119(13), e2115258119. <https://doi.org/10.1073/pnas.2115258119>
- Gubbins, D., & Roberts, N. (1983). Use of the frozen flux approximation in the interpretation of archaeological and palaeomagnetic data. *Geophysical Journal International*, 73(3), 675–687. <https://doi.org/10.1111/j.1365-246x.1983.tb03339.x>
- Hammer, M. D., & Finlay, C. C. (2018). Local averages of the core–mantle boundary magnetic field from satellite observations. *Geophysical Journal International*, 216(3), 1901–1918. <https://doi.org/10.1093/gji/ggy515>
- Hammer, M. D., Finlay, C. C., & Olsen, N. (2022). Secular variation signals in magnetic field gradient tensor elements derived from satellite-based geomagnetic virtual observatories. *Geophysical Journal International*, 229(3), 2096–2114. <https://doi.org/10.1093/gji/ggac004>
- Holme, R., & de Viron, O. (2013). Characterization and implications of intradecadal variations in length of day. *Nature*, 499(7457), 202–204. <https://doi.org/10.1038/nature12282>
- Holme, R., James, M. A., & Lühr, H. (2005). Magnetic field modelling from scalar-only data: Resolving the Backus effect with the equatorial electrojet. *Earth Planets and Space*, 57(12), 1203–1209. <https://doi.org/10.1186/bf03351905>
- Holme, R., Olsen, N., & Bairstow, F. L. (2011). Mapping geomagnetic secular variation at the core–mantle boundary. *Geophysical Journal International*, 186(2), 521–528. <https://doi.org/10.1111/j.1365-246x.2011.05066.x>
- Jackson, A. (1997). Time-dependency of tangentially geostrophic core surface motions. *Physics of the Earth and Planetary Interiors*, 103(3–4), 293–311. [https://doi.org/10.1016/s0031-9201\(97\)00039-3](https://doi.org/10.1016/s0031-9201(97)00039-3)
- Jackson, A., & Finlay, C. C. (2007). Geomagnetic secular variation and its applications to the core. *Treatise on Geophysics*, 5, 147–193. <https://doi.org/10.1016/b978-044452748-6.00090-0>
- Jackson, A., Jonkers, A. R. T., & Walker, M. R. (2000). Four centuries of geomagnetic secular variation from historical records. *Philosophical Transactions of the Royal Society of London A*, 358(1768), 957–990. <https://doi.org/10.1098/rsta.2000.0569>
- Kloss, C., & Finlay, C. C. (2019). Time-dependent low-latitude core flow and geomagnetic field acceleration pulses. *Geophysical Journal International*, 217(1), 140–168. <https://doi.org/10.1093/gji/ggy545>
- Langel, R. A. (1974). Near-Earth magnetic disturbance in total field at high latitudes, summary of data from OGO 2, 4, and 6. *Journal of Geophysical Research*, 79(16), 2363–2371. <https://doi.org/10.1029/ja079i016p02363>
- Laundal, K. M., & Richmond, A. D. (2017). Magnetic Coordinate systems. *Space Science Reviews*, 206, 27–59. <https://doi.org/10.1007/s11214-016-0275-y>
- Le Huy, M., Alexandrescu, M., Hulot, G., & Le Mouél, J.-L. (1998). On the characteristics of successive geomagnetic jerks. *Earth Planets and Space*, 50(9), 723–732. <https://doi.org/10.1186/bf03352165>
- Lesur, V., Wardinski, I., Hamoudi, M., & Rother, M. (2010). The second generation of the GFZ reference internal magnetic model: Grimm-2. *Earth Planets and Space*, 62(10), 6–773. <https://doi.org/10.5047/eps.2010.07.007>

- Lesur, V., Wardinski, I., Rother, M., & Manda, M. (2008). GRIMM: The GFZ reference internal magnetic model based on vector satellite and observatory data. *Geophysical Journal International*, 173(2), 382–394. <https://doi.org/10.1111/j.1365-246x.2008.03724.x>
- Macmillan, S., & Olsen, N. (2013). Observatory data and the Swarm mission. *Earth Planets and Space*, 1356–1358.
- Malin, S. R. C., Hodder, B. M., & Barraclough, D. R. (1983). Geomagnetic secular variation: A jerk in 1970. In J. O. Cardús (Ed.), *Scientific contributions in commemoration of EBRO observatory's 75th anniversary* (pp. 239–256).
- Manda, M., Holme, R., Pais, A., Pinheiro, K., Jackson, A., & Verbanac, G. (2010). Geomagnetic jerks: Rapid core field variations and core dynamics. *Space Science Reviews*, 155(1–4), 147–175. <https://doi.org/10.1007/s11214-010-9663-x>
- Matzka, J., Stolle, C., Yamazaki, Y., Bronkalla, O., & Morschhauser, A. (2021). The geomagnetic Kp index and derived indices of geomagnetic activity. *Space Weather*, 19. <https://doi.org/10.1029/2020SW002641>
- Olsen, N. (2002). A model of the geomagnetic field and its secular variation for epoch 2000 estimated from Ørsted data. *Geophysical Journal International*, 149(2), 454–462. <https://doi.org/10.1046/j.1365-246x.2002.01657.x>
- Olsen, N., & Manda, M. (2007). Investigation of a secular variation impulse using satellite data: The 2003 geomagnetic jerk. *Earth and Planetary Science Letters*, 255(1–2), 94–105. <https://doi.org/10.1016/j.epsl.2006.12.008>
- Olsen, N., & Manda, M. (2008). Rapidly changing flows in the earth's core. *Nature Geoscience*, 1(6), 390–394. <https://doi.org/10.1038/ngeo203>
- Olsen, N., Hulot, G., Lesur, V., Finlay, C. C., Beggan, C., Chulliat, A., et al. (2015). The Swarm initial field model for the 2014 geomagnetic field. *Geophysical Research Letters*, 42(4), 1092–1098. <https://doi.org/10.1002/2014gl062659>
- Olsen, N., Lühr, H., Finlay, C. C., Sabaka, T. J., Michaelis, I., Rauberg, J., & Tøffner-Clausen, L. (2014). The CHAOS-4 geomagnetic field model. *Geophysical Journal International*, 197(2), 817–819. <https://doi.org/10.1093/gji/ggu033>
- Olsen, N., Lühr, H., Sabaka, T. J., Manda, M., Rother, M., Tøffner-Clausen, L., & Choi, S. (2006). CHAOS — A model of the earth's magnetic field derived from CHAMP, Ørsted, and SAC-C magnetic satellite data. *Geophysical Journal International*, 166(1), 67–75. <https://doi.org/10.1111/j.1365-246x.2006.02959.x>
- Pinheiro, K., Jackson, A., & Finlay, C. (2011). Measurements and uncertainties of the occurrence time of the 1969, 1978, 1991, and 1999 geomagnetic jerks. *Geochemistry, Geophysics, Geosystems*, 12(10), Q10015. <https://doi.org/10.1029/2011gc003706>
- Sabaka, T. J., Olsen, N., & Purucker, M. E. (2004). Extending comprehensive models of the Earth's magnetic field with ørsted and champ data. *Geophysical Journal International*, 159(2), 521–547. <https://doi.org/10.1111/j.1365-246x.2004.02421.x>
- Stockmann, R., Christiansen, F., Olsen, N., & Jackson, A. (2015). POGO satellite orbit corrections: An opportunity to improve the quality of the geomagnetic field measurements? *Earth Planets and Space*, 67, 1–3. <https://doi.org/10.1186/s40623-015-0254-7>
- Torta, J. M., Pavón-Carrasco, F. J., Marsal, S., & Finlay, C. C. (2015). Evidence for a new geomagnetic jerk in 2014. *Geophysical Research Letters*, 42(19), 7933–7940. <https://doi.org/10.1002/2015gl065501>
- Walker, M. R., & Jackson, A. (2000). Robust modelling of the Earth's magnetic field. *Geophysical Journal International*, 143(3), 799–808. <https://doi.org/10.1046/j.1365-246x.2000.00274.x>